

Beam size and position measurement based on logarithm processing algorithm in HLS II^{*}

Chao-Cai Cheng(程超才)¹⁾ Bao-Gen Sun(孙葆根)²⁾ Yong-Liang Yang(杨永良) Ze-Ran Zhou(周泽然)
 Ping Lu(卢平) Fang-Fang Wu(吴芳芳) Ji-Gang Wang(王季刚) Kai Tang(唐凯)
 Qing Luo(罗箐) Hao Li(李皓) Jia-Jun Zheng(郑佳俊) Qing-Ming Duan(段青明)

National Synchrotron Radiation Laboratory, University of Science and Technology of China, Hefei 230029, China

Abstract: A logarithm processing algorithm to measure beam transverse size and position is proposed and preliminary experimental results in Hefei Light Source II (HLS II) are given. The algorithm is based on only 4 successive channels of 16 anode channels of multianode photomultiplier tube (MAPMT) R5900U-00-L16, which has typical rise time of 0.6 ns and effective area of 0.8×16 mm for a single anode channel. In the paper, we first elaborate the simulation results of the algorithm with and without channel inconsistency. Then we calibrate the channel inconsistency and verify the algorithm using a general current signal processor Libera Photon in a low-speed scheme. Finally we get turn-by-turn beam size and position and calculate the vertical tune in a high-speed scheme. The experimental results show that measured values fit well with simulation results after channel differences are calibrated, and the fractional part of the tune in vertical direction is 0.3628, which is very close to the nominal value 0.3621.

Keywords: logarithm processing algorithm, beam size and position, multianode photomultiplier tube, channel inconsistency

PACS: 29.20.db, 29.85.Ca, 29.90.+r **DOI:** 10.1088/1674-1137/40/4/047004

1 Introduction

In an electron storage ring, machine parameters, such as transverse impedance [1] deduced by both dipolar and quadrupolar tune shifts, and injection mismatch [2] can be studied by acquiring the turn-by-turn beam size and position. In general, beam transverse profile measurement based on visible light from synchrotron radiation (SR) is widely used [3]. A CCD can be used to provide an online continuous beam size and position measurement, but a conventional CCD has a long exposure time and a very low frame rate. In Hefei Light Source II (HLS II), a CCD camera has been installed to measure the beam profile and to monitor the machine status. The CCD camera has a maximum frame rate of 205 Hz at its full resolution (640×480). The electron beam goes through about 22k revolutions in the ring during a single frame acquisition. As a result, the measurement results are the average of multiple bunches in multiple turns.

In order to track the beam size and position of a single bunch, it is necessary to acquire transient light intensity information using a high speed photodetector and data acquisition system to ensure that the transformed light

pulse are not piled up along the pulse train. The typical schemes are VEPP-4M [4] and CESR-c [5], which calculate the turn-by-turn or bunch-by-bunch beam size and position to study beam-beam interaction, beam dynamics, etc. In these measurement schemes, dozens of channel photocurrents, up to 16 or 32, are sampled in parallel to fit the shape of Gaussian beam spot, which increase the costs and complexities. Therefore, we put forward a logarithm processing algorithm to calculate the beam size and position which needs only 4 successive channels, and carry out some experiments to verify the algorithm.

2 Principle of the measurement system

At present there are 4 applications in the visible light diagnostic beamline located at the 15° outlet of the bending magnet in HLS II. Figure 1 shows a block diagram of the measurement system with the CCD and vertical multianode photomultiplier tube (MAPMT). Synchrotron radiation is first reflected by a water-cooled Oxygen Free Copper (OFC) mirror in the vacuum chamber. Then the visible light passes through several mirrors and a main focusing lens with magnification of 1 before

Received 4 August 2015, Revised 26 November 2015

^{*} Supported by National Natural Science Foundation of China (11005105, 11175173)

1) E-mail: ccc1989@mail.ustc.edu.cn

2) E-mail: bgsun@ustc.edu.cn

©2016 Chinese Physical Society and the Institute of High Energy Physics of the Chinese Academy of Sciences and the Institute of Modern Physics of the Chinese Academy of Sciences and IOP Publishing Ltd

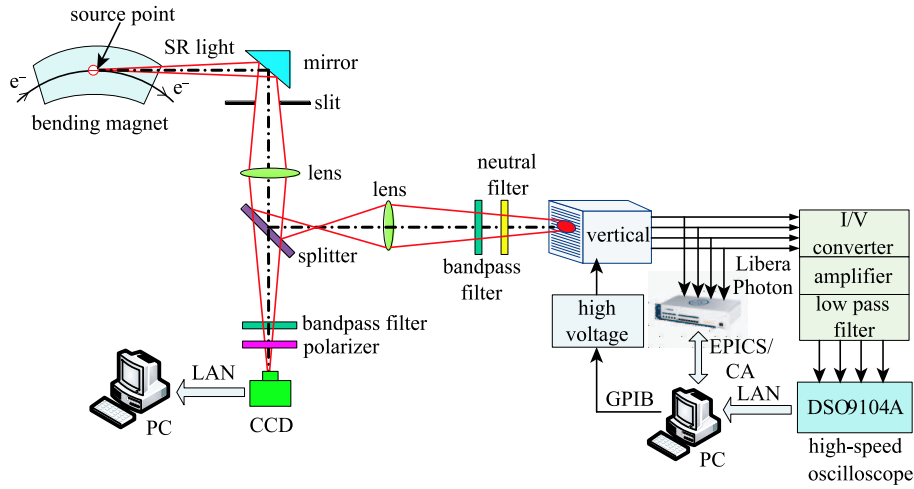


Fig. 1. (color online) Block diagram of the measurement system.

reaching the optical table. The MAPMT and CCD [6] share the same magnification of 2 by the front-end optical path. After that the beam spot reaches the horizontal and vertical MAPMT cathode with magnification of 6 and magnification of 24 respectively to ensure the beam size matches the channel width of MAPMT. Magnification can be altered to meet the needs of different machine statuses. The two MAPMTs are fixed on a three-dimensional translation stage so as to find the image plane conveniently. A front-end circular slit constrains the opening angle of SR within ± 3.8 mrad to decrease the depth of field error and diffraction error [7]. A band pass filter with 500 nm peak wavelength and 10 nm full width at half maximum (FWHM) is used to allow quasi-monochromatic light to get to the sensitive area of the MAPMT.

The measurement system works in two schemes. In the low-speed scheme, the photocurrents of 4 successive channels are sampled by a general current signal processor Libera Photon [8]. Then they are sent to a remote PC through EPICS/CA [9] where we can calibrate the channel inconsistency, implement the logarithm processing algorithm and control the negative high voltage to protect the MAPMT. In the high-speed scheme, photocurrents are first conditioned by analog front-end electronics (AFE) including current to voltage conversion, preamplifier and low pass filter. Then the transformed signals are sampled simultaneously by a high speed oscilloscope DSO9104A [10] and acquired over Local Area Network (LAN) by a remote PC where we can calculate turn-by-turn beam size and position, perform Fast Fourier Transform (FFT), etc.

3 Logarithm processing algorithm [11]

As the SR light irradiated by the electron beam from the bending magnet in a storage ring has a Gaussian dis-

tribution, we assume the SR light intensity distribution function $\Phi(x)$ is

$$\Phi(x) = \Phi_0 \exp \left[- \left(\frac{x - \delta}{\sqrt{2}\sigma} \right)^2 \right], \quad (1)$$

where Φ_0 is the maximum light intensity, δ is the beam displacement (where the center of the beam spot is offset from the specified center of the MAPMT) and σ is the beam size.

Based on the assumption of Gaussian distribution, the SR light intensity distribution at the MAPMT is shown in Fig. 2. The rectangular regions of I_1 , I_2 , I_3 and I_4 represent effective photosensitive areas with a 0.2 mm gap between them.

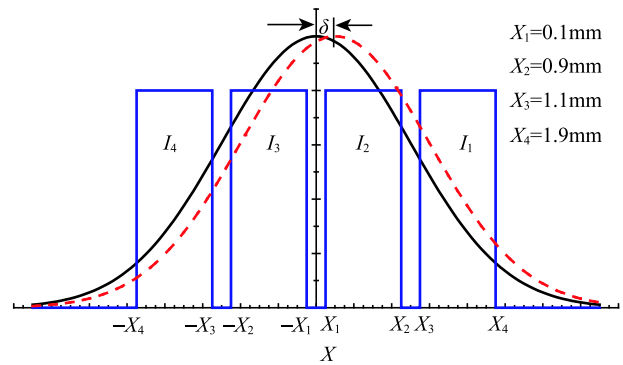


Fig. 2. (color online) Light intensity distribution at MAPMT.

Photocurrents of I_1 , I_2 , I_3 and I_4 , which are derived from 4 successive channels, are proportional to the integral of light intensity and can be expressed by the subtraction of the two error functions shown in Eq. (2).

$$\begin{cases} I_1 = \int_{x_3}^{x_4} \Phi(x) dx = I_0 \left[\operatorname{erf} \left(\frac{x_4 - \delta}{\sqrt{2}} \right) - \operatorname{erf} \left(\frac{x_3 - \delta}{\sqrt{2}} \right) \right], \\ I_2 = \int_{x_1}^{x_2} \Phi(x) dx = I_0 \left[\operatorname{erf} \left(\frac{x_2 - \delta}{\sqrt{2}} \right) - \operatorname{erf} \left(\frac{x_1 - \delta}{\sqrt{2}} \right) \right], \\ I_3 = \int_{-x_2}^{-x_1} \Phi(x) dx = I_0 \left[\operatorname{erf} \left(\frac{-x_1 - \delta}{\sqrt{2}} \right) - \operatorname{erf} \left(\frac{-x_2 - \delta}{\sqrt{2}} \right) \right], \\ I_4 = \int_{-x_4}^{-x_3} \Phi(x) dx = I_0 \left[\operatorname{erf} \left(\frac{-x_3 - \delta}{\sqrt{2}} \right) - \operatorname{erf} \left(\frac{-x_4 - \delta}{\sqrt{2}} \right) \right], \end{cases} \quad (2)$$

where $\operatorname{erf}(x) = \frac{2}{\sqrt{\pi}} \int_0^x e^{-t^2} dt$, $x_1=0.1$ mm, $x_2=0.9$ mm,

$x_3=1.1$ mm, $x_4=1.9$ mm and I_0 is the maximum anode photocurrent.

3.1 Ideal case

In the ideal condition, the 4 continuous channels have the same response characteristic and we define the ideal size signal $S_{\text{in}}(\sigma, \delta)$ and the ideal position signal $P_{\text{in}}(\sigma, \delta)$ as

$$\begin{cases} S_{\text{in}}(\sigma, \delta) = [\ln(I_2 I_3 / I_1 I_4)]^{-1/2}, \\ P_{\text{in}}(\sigma, \delta) = \frac{\ln(I_1 I_2 / I_3 I_4)}{\ln(I_2 I_3 / I_1 I_4)}. \end{cases} \quad (3)$$

Substituting the integral results shown in Eq. (2) into Eq. (3) and simplifying it, we can obtain how the size and position signal vary with size and position, as illustrated in Fig. 3. When the beam size increases from 0.2 mm to 2.0 mm without beam displacement, the size sig-

nal $S_{\text{in}}(\sigma, \delta)$ has a good linear relation with the beam size. The linear fitting equation can be expressed by $S_{\text{in}}(\sigma) = 0.04 + 0.69\sigma$. When the beam size varies within 0.8–2.0 mm, beam displacement has an effect on the normalized size signal within 1%. Meanwhile, the position signal $P_{\text{in}}(\sigma, \delta)$ has a good linear relation with the beam displacement when beam displacement varies from –2.0 mm to 2.0 mm. The linear fitting equation is $P_{\text{in}}(\delta) = 2\delta$. Furthermore, the beam size has an impact on the position signal sensitivity within 1%.

From the above simulation results, we can get the approximate equations expressed as

$$\begin{cases} S_{\text{in}}(\sigma, \delta) \approx S_{\text{in}}(\sigma) = 0.04 + 0.69\sigma, \\ P_{\text{in}}(\sigma, \delta) \approx P_{\text{in}}(\sigma) = 2\delta. \end{cases} \quad (4)$$

3.2 Non-ideal case

Given that channel inconsistency results from anode uniformity and cross-talk among channels, we introduce the channel gain factor g_i ($i = 1, 2, 3, 4$) to correct channel inconsistency based on linear approximation, as shown in Eq. (5).

$$\begin{cases} \hat{S}_{\text{in}}(\sigma, \delta) = \left[\ln(\hat{I}_2 \hat{I}_3 / \hat{I}_1 \hat{I}_4) \right]^{-1/2} \\ = [\ln(g_2 g_3 / g_1 g_4) + \ln(I_2 I_3 / I_1 I_4)]^{-1/2}, \\ \hat{P}_{\text{in}}(\sigma, \delta) = \frac{\ln(\hat{I}_1 \hat{I}_2 / \hat{I}_3 \hat{I}_4)}{\ln(\hat{I}_2 \hat{I}_3 / \hat{I}_1 \hat{I}_4)} \\ = \frac{\ln(g_1 g_2 / g_3 g_4) + \ln(I_1 I_2 / I_3 I_4)}{\ln(g_2 g_3 / g_1 g_4) + \ln(I_2 I_3 / I_1 I_4)}, \end{cases} \quad (5)$$

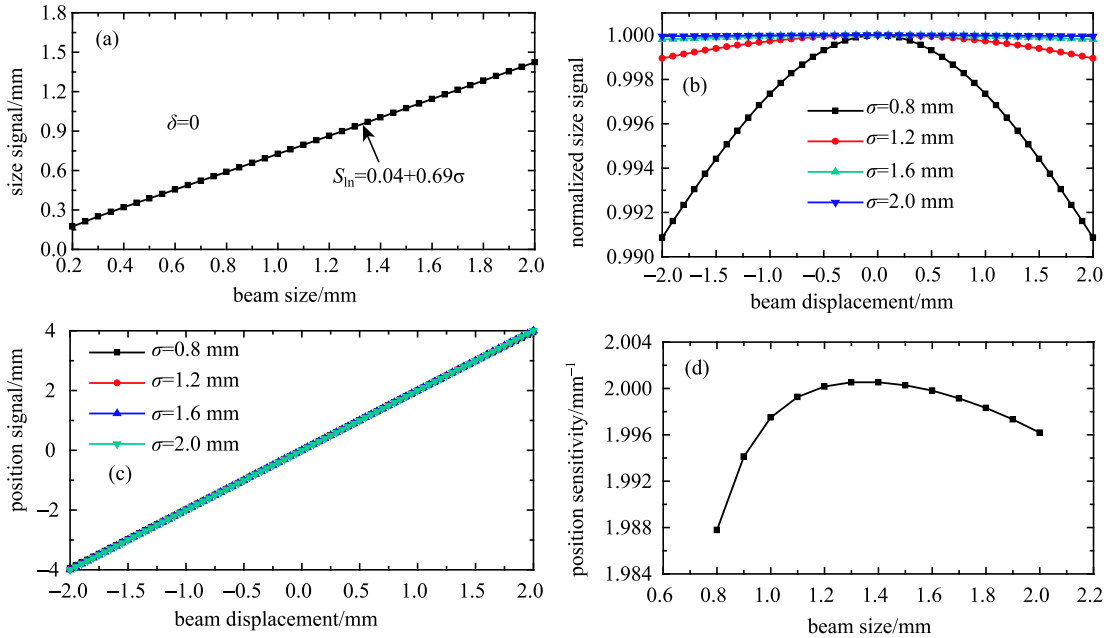


Fig. 3. (color online) The simulation results of ideal beam size and position signal in different conditions: (a) size signal versus beam size when $\delta=0$ mm; (b) normalized size signal versus beam displacement when $\sigma=0.8$ –2.0 mm; (c) position signal versus beam displacement when $\sigma=0.8$ –2.0 mm; (d) position signal sensitivity versus beam size.

where $\hat{S}_{\text{in}}(\sigma, \delta)$ is the actual size signal, $\hat{P}_{\text{in}}(\sigma, \delta)$ is the actual position signal, and $\hat{I}_i = g_i I_i$ ($i = 1, 2, 3, 4$) represents actual anode photocurrent with channel inconsistency.

If we define $d_s = \ln(g_2 g_3 / g_1 g_4)$, $d_p = \ln(g_1 g_2 / g_3 g_4)$ and put Eq. (4) into Eq. (5), we get:

$$\begin{cases} \hat{S}_{\text{in}}(\sigma, \delta) \approx S_{\text{in}}(\sigma) \left[1 + \tilde{d}_s S_{\text{in}}^2(\sigma) \right]^{-1/2}, \\ \hat{P}_{\text{in}}(\sigma, \delta) \approx P_{\text{in}}(\delta) \left[1 + \tilde{d}_s S_{\text{in}}^2(\sigma) \right]^{-1} + \\ \tilde{d}_p S_{\text{in}}^2(\sigma) \left[1 + \tilde{d}_s S_{\text{in}}^2(\sigma) \right]^{-1}, \end{cases} \quad (6)$$

where \tilde{d}_s and \tilde{d}_p are gain correction factors.

According to Eq. (6), we know that the actual position signal has a good linear relation with the beam position, but the actual size signal presents a huge non-linearity with the beam size. In addition, \tilde{d}_s and \tilde{d}_p can be deduced by the slope and intercept of $\hat{P}_{\text{in}}(\sigma, \delta)$ if beam size and magnification can be acquired in advance. Hence, modified size signal $\tilde{S}_{\text{in}}(\sigma, \delta)$ and modified position signal $\tilde{P}_{\text{in}}(\sigma, \delta)$ can be expressed as

$$\begin{cases} \tilde{S}_{\text{in}}(\sigma, \delta) = \left[\ln(\hat{I}_2 \hat{I}_3 / \hat{I}_1 \hat{I}_4) - \tilde{d}_s \right]^{-1/2}, \\ \tilde{P}_{\text{in}}(\sigma, \delta) = \frac{\ln(\hat{I}_1 \hat{I}_2 / \hat{I}_3 \hat{I}_4) - \tilde{d}_p}{\ln(\hat{I}_2 \hat{I}_3 / \hat{I}_1 \hat{I}_4) - \tilde{d}_s}. \end{cases} \quad (7)$$

4 Experimental results

4.1 Low-speed scheme

In the low-speed scheme, the horizontal measurement results are described. In order to simulate the movement of beam center, we move the three-dimensional translation stage for horizontal MAPMT horizontally. The movement range is from 13.0 mm to 16.8 mm with 0.1 mm step. The process of movement is very short, so the beam size measured by CCD remains unchanged.

Figure 4 shows how the average anode output current varies with the change in position. CH4, CH5, CH6 and CH7 correspond to channel number 4, 5, 6 and 7 respectively. When the horizontal translation stage increases, the average anode current of CH4 and CH5 increases and it is just opposite for CH6 and CH7, which roughly indicates that the center of the beam spot is moving from CH7 to CH4. In the middle point of 14.9 mm, the anode current of CH4 and CH7 are approximately the same, and the same is true for CH5 and CH6. Thus this position can be thought to be the absolute center.

Putting the average anode current into Eq. (5), we can get how the actual position signal varies with the simulated beam displacement shown in Fig. 5. The horizontal coordinate axis has been adjusted by subtracting the absolute center. Applying linear fitting to the raw

discrete points, we can get the fitting equation with slope of 1.79 and intercept of -0.12 . The actual position signal has a linear relation with simulated beam displacement as described in Eq. (6). However, the fitting curve does not cross the point $(0, 0)$, and the slope is not equal to the simulation result in the ideal case shown in Fig. 3(c). The difference mainly comes from the channel inconsistency and must be calibrated.

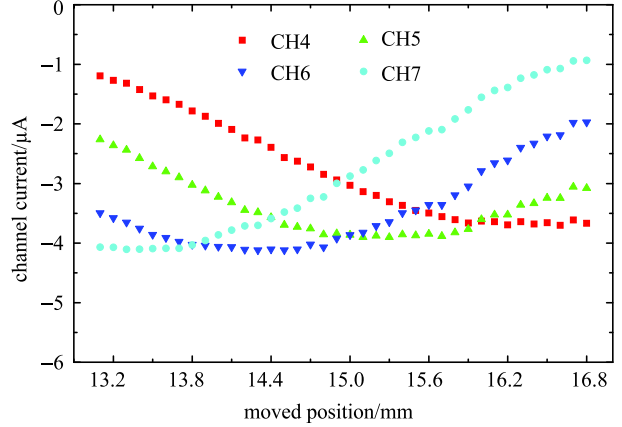


Fig. 4. (color online) Average anode current of 4 successive channels.

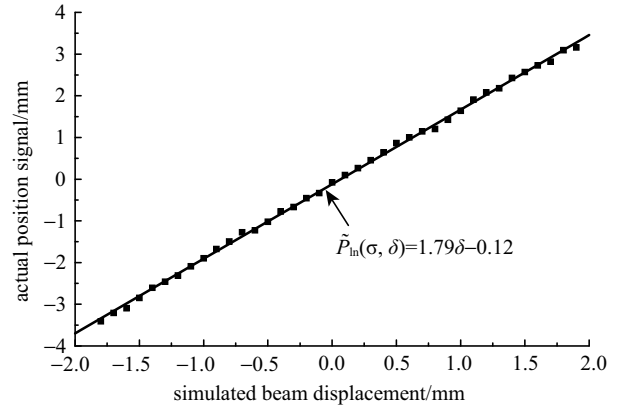


Fig. 5. Actual position signal with channel inconsistency.

Substituting the beam size at the horizontal MAPMT cathode into Eq. (6), we can get the measured gain correction factors $d_s = 0.059$ and $d_p = -0.068$ based on the fitting equation shown in Fig. 5. As a consequence, the relationship between the modified position signal and the simulated position can be illustrated in Fig. 6. Linear fitting results show that the modified position signal has a good linear relation with the simulated beam displacement and the fitting curve crosses point $(0, 0)$ which agrees well with the simulation results shown in Fig. 3(c).

The beam size at the source point calculated by the direct equation in Eq. (5), the modified equation in Eq. (7) and the linear magnification of both horizontal and vertical directions is illustrated in Fig. 7. Although

the modified beam size signal, which is proportional to beam size, should remain almost unchanged according to Fig. 3(b), direct and modified beam size gradually decrease when the beam center is moved from -1.8 mm to 1.9 mm. The modified beam size is closer, however, to the nominal value 0.33 mm measured by the CCD and is more reliable.

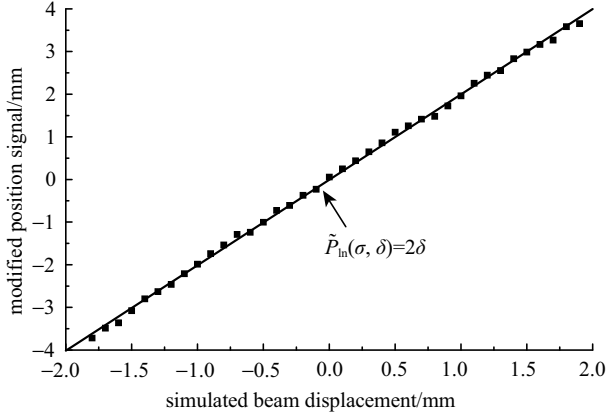


Fig. 6. Modified position signal.

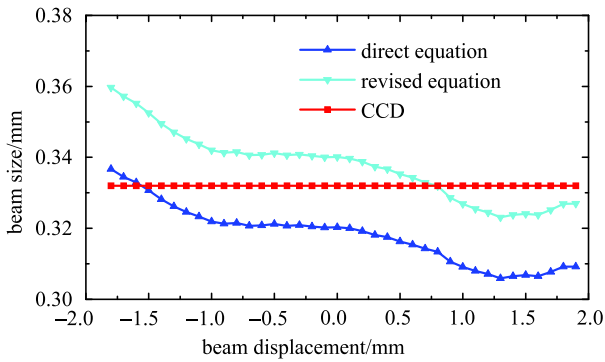


Fig. 7. (color online) Direct and modified beam size.

4.2 High-speed scheme

In the high-speed scheme, we take the vertical measurement results as an example. A single bunch fills in the storage ring with 3 mA beam current and the electron beam is excited by a swept frequency signal which comes from the tracking generator module in the spectrum analyzer. Signals from AFE are continuously sampled at $500\,000$ points with 10 GS/s sample rate for 4 channels. An external trigger signal with a frequency of 4.534 MHz synchronized with the revolution frequency is applied to keep pace with the pulse signal. Figure 8 shows the peak values extracted from results of cubic spline interpolation of raw data points to avoid the phase shift since the sample frequency is not an integer multiple of the revolution frequency. CH8, CH9, CH10 and CH11 correspond to channel number 8, 9, 10 and 11 respectively. The peak values of CH9 and CH10 are larger than CH8

and CH11 indicating that beam center is located between the CH9 and CH10, which satisfies the conditions of the algorithm.

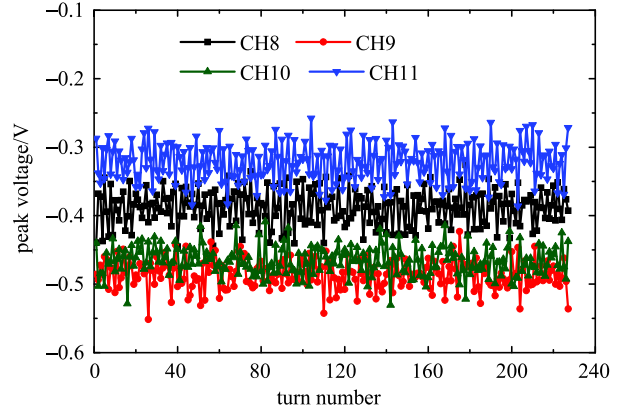


Fig. 8. (color online) Peak values of 227 turns for 4 successive channels.

Applying FFT to the interpolated data and enlarging the view of spectrum of CH9 in frequency range of 0 Hz to 10 MHz shown in Fig. 9, we can clearly see vertical synchronous oscillation sidebands appear at frequencies of 1.62 MHz, 2.90 MHz, 6.16 MHz and 7.44 MHz, except for two main harmonic components at the frequencies of 4.53 MHz and 9.06 MHz, which are roughly equal to the integral multiple of the revolution frequency. These sideband elements result from the interactions between the synchronous light and slit. In HLS II, frequencies at 1.62 MHz and 6.16 MHz correspond to betatron oscillation in vertical direction, and frequencies at 2.90 MHz and 7.44 MHz are the mirrored components of vertical betatron oscillation.

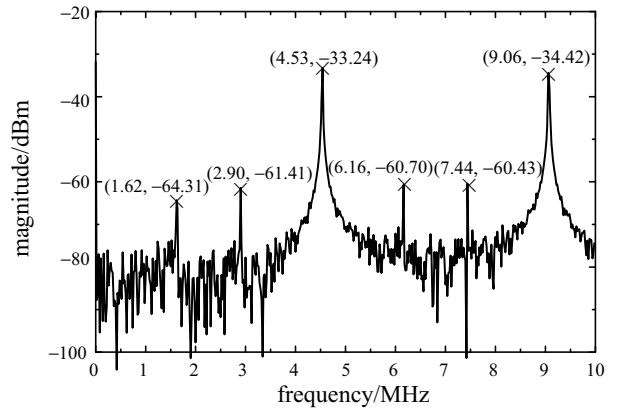


Fig. 9. Spectrum of CH9.

With the channel inconsistency calibrated and the logarithm processing algorithm adopted, we can get the turn-by-turn beam size and position of SR light spot shown in Fig. 10. From Fig. 10(a), beam size varies between 64.5 μm and 93.5 μm with the average of 76.4 μm . From Fig. 10(b), beam position varies between -8.2

μm and $22.6 \mu\text{m}$ and the average value is $8.0 \mu\text{m}$. Meanwhile, we record the beam size with the CCD which tells that the beam size is about $70.0 \mu\text{m}$. The average result of beam size is larger than the size obtained from the CCD by about 8%. Several factors may lead to the system error: 1) the magnification is not exactly equal to

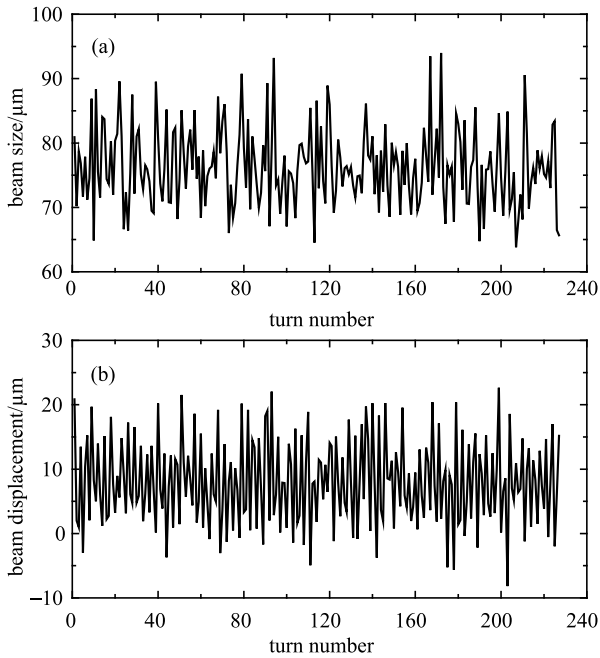


Fig. 10. Beam size and position for 227 turns with excitation: (a) beam size; (b) beam position.

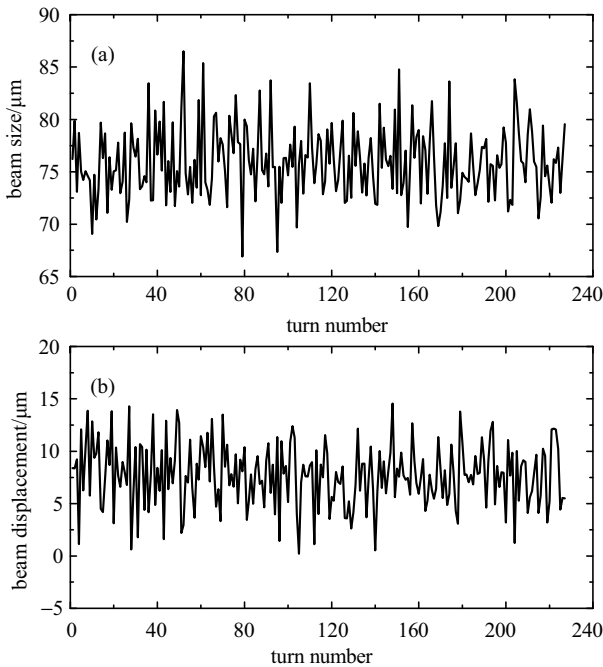


Fig. 11. Beam size and position for 227 turns without excitation: (a) beam size; (b) beam position.

the design value, 2) the MAPMT cathode is not located exactly in the image plane and 3) the channel consistency is not totally revised. These factors will be checked and solved one by one in the future.

Meanwhile, we measure the beam size and position in routine mode when the tracking generator is turned off. Figure 11 shows the measured results of turn-by-turn beam size and position without excitation. From Fig. 11(a), the average beam size is $75.9 \mu\text{m}$ and the standard deviation is $3.4 \mu\text{m}$. According to Fig. 11(b), the average beam position and the standard deviation are $7.7 \mu\text{m}$ and $3.0 \mu\text{m}$ respectively. So the resolution of the whole system for both position and size is better than $3.5 \mu\text{m}$.

Applying FFT to the turn-by-turn beam position and getting rid of the dc component, we can see a peak signal at the frequency of 1.645 MHz corresponding to the vertical betatron oscillation sideband shown in Fig. 12. So the vertical fractional tune is 0.3628 with 4.534 MHz revolution frequency. The measured result is in good agreement with the nominal value 0.3621 .

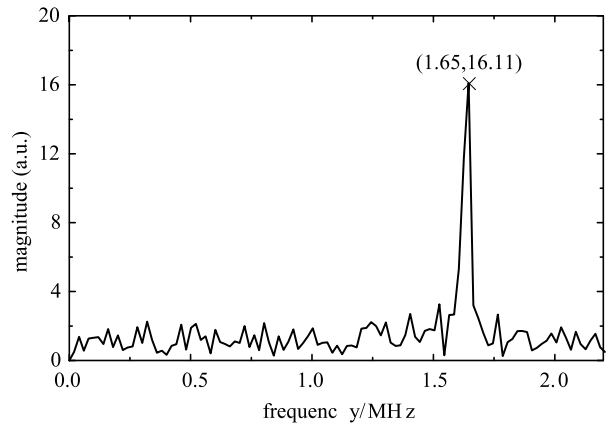


Fig. 12. Spectrum of turn-by-turn position.

5 Conclusion

A logarithm processing algorithm used to calculate beam transverse size and position based on SR light in HLS II is developed and preliminary experimental results are given. The measurement results are in good agreement with the simulation results after the channel inconsistency is calibrated. Vertical fractional tune of 0.3628 is obtained according to the turn-by-turn beam position, which is very close to the nominal value 0.3621 . More experiments will be conducted in multiple bunches filling mode, and effective ways to excite an obvious change of beam size should be applied to study beam instability and beam dynamics.

References

- 1 S. Sakanaka, T. Mitsuhashi, and T. Obina, *Phys. Rev. ST Accel. Beams*, **8**: 042801 (2005)
- 2 T. Naito, Y. Hashimoto, H. Hayano et al, Beta-Matching and Damping Observation by SR Monitor at ATF DR, in *Proceedings of EPAC 1998*, Stockholm, Sweden, p. 1576
- 3 G. Kube, Review of Synchrotron Radiation based Diagnostics for Transverse Profile Measurements, in *Proceedings of DIPAC 2007*, Venice, Italy, p. 6
- 4 A. V. Bogomyagkov, V. F. Gurko, A. N. Zhuravlev et al, *Rev. Sci. Instrum.*, **78**: 043305 (2007)
- 5 M. Palmer, J. Dobbins, D. Hartill et al, Design and Implementation of an Electron and Positron Multibunch Turn-By-Turn Vertical Beam Profile Monitor in CESR, in *Proceedings of PAC 2007*, Albuquerque, New Mexico, p. 4081
- 6 K. Tang, J. G. Wang, B. G. Sun et al, *High Power Laser and Particle Beams*, **27**: 075101 (2015) (in Chinese)
- 7 J. A. Clarke, A Review of Optical Diagnostics Techniques for Beam Profile Measurements, in *Proceedings of EPAC 1994*, Daresbury, UK, p. 1643
- 8 P. Leban, D. Tinta, and C. Pradervand, Photon Beam Position Measurements Using CVD Diamond based Beam Position Sensor and Libera Photon at Swiss Light Source, in *Proceedings of IPAC 2010*, Kyoto, Japan, p. 1077
- 9 <http://www.aps.anl.gov/epics/>
- 10 <http://literature.cdn.keysight.com/litweb/pdf/5990-3746EN.pdf>, retrieved 12th October 2014
- 11 C. C. Cheng, Y. Y. Xiao, B. G. Sun et al, A New Method of Acquiring Fast Beam Transversal Profile in the Storage Ring, in *Proceedings of IPAC 2013*, Shanghai, China, p. 556